

Experimental characterization and modelling of aluminum alloy AA3103 for complex single and double strain-path changes

Jisheng Qin ^a, Bjørn Holmedal ^a and Odd Sture Hopperstad ^{b,c}

^aDepartment of Materials Science and Engineering, Norwegian University of Science and Technology (NTNU), NO-7491 Trondheim, Norway

^bStructural Impact Laboratory (SIMLab), Department of Structural Engineering, NTNU, NO-7491 Trondheim, Norway

^cCentre for Advanced Structural Analysis (CASA), NTNU, NO-7491 Trondheim, Norway

qin_jisheng@hotmail.com, bjorn.holmedal@ntnu.no, odd.hopperstad@ntnu.no

Corresponding author: Jisheng Qin, Tel.: +1 6145866766

Abstract

The stress-strain behavior of the aluminum alloy AA3103 subjected to single and double strain-path changes (SPCs) is studied experimentally. The experimental program includes compression-tension, tension-tension, rolling-tension and tension-rolling-tension tests. The considered AA3103 plate exhibits plastic anisotropy, a strong Bauschinger effect with hardening stagnation after strain reversal, cross-hardening and permanent softening after orthogonal SPCs in the tension-tension tests. However, when instead the orthogonal SPCs are obtained by rolling-tension tests, cross-softening is observed. The same behavior is seen in more complex tension-rolling-tension tests. Three state-of-the-art advanced plasticity models are used in an attempt to model the experimentally observed behavior. These models all account for plastic anisotropy and transient effects after SPCs, using a microstructure deviator tensor to describe a fading memory of the deformation history. While the models successfully describe the behavior after strain reversals, they fail to represent the behavior after orthogonal SPCs. It is concluded that the Schmitt angle, on which the current models depend, is not sufficient for a fundamental description of SPCs for the considered AA3103 alloy.

Keywords: A. Yield condition; B. Anisotropic material; B. elastic-plastic material; B. Constitutive behavior; Strain-path change.

1. Introduction

Strain-path changes (SPCs) often occur in sheet metal forming processes. The SPC modifies the hardening behavior and may reduce the ductility of the material. Hence, it is of interest to systematically evaluate the properties of a sheet metal subjected to SPCs. The plastic anisotropy of metals with respect to yield strength, work hardening and plastic flow can be influenced by many factors on different length scales. In steel and aluminum, the main irreversible deformation mechanism is slip (Lubliner, 2008). The two important consequences of the slip activity are the formation of deformation microstructures with a variation both between grains and within grains, and a deformation texture determined by changes in grain orientations. In pure iron or aluminum, dislocations will form cell structures and subgrain boundary structures during straining at room temperature.

Constitutive models accounting for SPCs have been formulated either based on the continuum theory of plasticity or the theory of crystal plasticity. For the case of an IF-steel, a detailed microstructure evolution model and a corresponding crystal plasticity model were proposed by Peeters et al. (2001a, 2001b), from which it was concluded that the grain-scale substructure transiently distorts the yield locus (Peeters et al., 2002, 2001b), whereas the texture did not evolve significantly. Similar conclusions were drawn from the more generic crystal plasticity model proposed by Holmedal et al. (2008), which was applied successfully to aluminum alloys. These kinds of physically based models provide important ideas and understanding for formulating the phenomenological continuum plasticity models considered in this work.

Previous work on aluminum has shown that for a sequence of two strain paths, the behavior during the second strain path is highly dependent on the magnitude of the SPC (Holmedal et al., 2008; Qin et al., 2017a, 2017b; Satheesh Kumar and Raghu, 2015; Yoshida and Tsuchimoto, 2018). Changes of the direction of the plastic rate-of-deformation tensor \mathbf{D}^p or, alternatively, the deviatoric stress tensor $\boldsymbol{\sigma}'$ are used to define SPCs, being either continuous or abrupt. Schmitt et al. (1994) proposed to measure abrupt SPCs by

$$\cos \phi_D = \frac{\mathbf{D}_1^p : \mathbf{D}_2^p}{\|\mathbf{D}_1^p\| \|\mathbf{D}_2^p\|} \quad (1)$$

while Barlat et al. (2011) used instead

$$\cos \phi_\sigma = \frac{\boldsymbol{\sigma}'_1 : \boldsymbol{\sigma}'_2}{\|\boldsymbol{\sigma}'_1\| \|\boldsymbol{\sigma}'_2\|} \quad (2)$$

Here, ϕ_D and ϕ_σ are the two alternative Schmitt angles, and $\cos \phi_D$ and $\cos \phi_\sigma$ the corresponding Schmitt factors. The subscripts 1 and 2 refer to the strain path before and after the SPC, respectively, and $\|\mathbf{T}\| = \sqrt{T_{ij}T_{ij}}$ is the norm of the second order tensor \mathbf{T} . The value of the Schmitt factor $\cos \phi$ signifies the character of the SPC: $\cos \phi = 1$ for monotonic loading, $\cos \phi = -1$ for reversed loading and $\cos \phi = 0$ for purely orthogonal loading.

The Bauschinger effect (Bauschinger, 1881) occurs after reverse SPCs and is of great importance for simulation of springback in forming processes (Lee et al., 2012). A precise method for evaluating the Bauschinger effect is to perform tension tests after prestraining in compression. However, the sheet metal easily buckles under compression and special care must be taken to avoid this instability. Different types of anti-buckling devices and specimen geometries have been proposed to avoid buckling even at large compressive strains, e.g. Yoshida et al. (2002), Boger et al. (2005) and Cao et al. (2009). An alternative method is to use reverse simple shear tests (Barlat et al., 2011), but for anisotropic materials these tests are more complex to analyze because the transverse normal stress is not measured.

Besides the Bauschinger effect, SPCs may lead to other transient or permanent effects, such as transient cross-hardening or cross-softening, hardening stagnation and permanent softening. The cross-hardening effect occurs subsequent to orthogonal SPCs (Khan et al., 2010) and refers to a transient increase of the yield strength followed by strain softening and finally resumption of strain hardening. For some materials, cross-softening occurs after orthogonal SPCs (Ha et al., 2013). Hardening stagnation normally occurs subsequent to reverse SPCs and an inflection point of the stress-strain curve can be seen (Barlat et al., 2011; Mánik et al., 2015). Permanent softening refers to a permanently reduced stress level sometimes observed after SPCs (Liao et al., 2017).

In plasticity theory, the yield criterion is used in combination with the hardening rule to describe the various stress-strain behaviors after SPCs. Isotropic (Hershey, 1954; Tresca, 1864; Von Mises, 1913) and anisotropic (Banabic et al., 2000; Barlat et al., 2005; Barlat et al., 2003; Barlat and Lian, 1989; Hill, 1948) yield criteria are commonly adopted to describe yielding in materials with random texture and textured materials, respectively. In order to capture the Bauschinger effect, one or several backstress tensors can be incorporated into the yield

functions to model kinematic hardening (Mánik et al., 2015), while the other transient SPC effects require additional internal variables.

The Teodosiu-Hu model was designed to capture the transient SPC effects based on isotropic expansion and shrinkage of the yield surface after SPCs (Teodosiu and Hu, 1995). It has been employed and modified in a number of later studies to model the transient behavior after SPCs (Bouvier et al., 2005; Wang et al., 2008; Wang et al., 2006). Mánik et al. (2015) proposed a model (here labelled the MHH model), which is based on a similar approach as the Teodosiu-Hu model, i.e., by isotropic expansion of the yield surface combined with nonlinear kinematic hardening as a response to a SPC. The MHH model faithfully describes the behavior of commercially pure aluminum sheet metal subjected to reverse and orthogonal SPCs. However, the model cannot capture the trends of low carbon steel subjected to double SPCs (Qin et al., 2017b; Vincze et al., 2013). In a recent study, Qin et al. (2017a) proposed a distortional hardening model (here labelled the QHH model) which combines distortion of the yield surface with nonlinear isotropic and kinematic hardening, and showed that this model captured the typical behavior of low carbon steel subjected to double SPCs as well as the behavior of commercially pure aluminum, an extra deep drawing quality steel and a dual-phase steel after single SPCs.

Levkovitch and Svendsen (2007) proposed a distortional hardening model and accounted for the difference between the tensile and compressive strength. A method for distorting any “stable” homogeneous yield surface by compression or expansion with respect to one particular direction in the stress space was proposed by Barlat et al. (2011) as an alternative to kinematic hardening. The yield criterion thus obtained is referred to as the Homogeneous Anisotropic Hardening (HAH) model. The HAH model was further extended to model cross-hardening effects (Barlat et al., 2013) and enhanced to describe the features of low carbon steel subjected to double SPCs (Barlat et al., 2014). In order to model the hardening stagnation after reverse SPCs and the permanent softening after orthogonal SPC, the enhanced HAH model (Barlat et al., 2014) was further developed by Qin et al. (2017b). This latter version of the HAH model is used in the present study.

In the previous studies, the MHH, QHH and HAH models have been shown to describe the Bauschinger effect, the hardening stagnation and the permanent softening after reverse SPCs, and the orthogonal hardening and the permanent softening after orthogonal SPCs (Mánik et al., 2015; Qin et al., 2017a, 2017b). However, a systematic evaluation of these three models for a material with strong Bauschinger effect being subjected to reverse and complex

orthogonal SPCs has not been conducted. The AA3103 alloy is chosen in this work, because it shows a strong cross hardening response, similar to pure metals (Holmedal et al., 2008), but at the same time, it contains dispersoids formed during the homogenization treatment, and these particles are known to cause strong Bauschinger effects (Zhao and Holmedal, 2013). The stress-strain behavior of aluminum alloy AA3103 sheets subjected to single and double SPCs is studied experimentally, and the MHH, QHH and HAH models are evaluated against the experimental data for single SPCs. Using the experimental data from the compression-tension and tension-tension tests to calibrate the constitutive models, the rolling-tension tests are used to assess the credibility of the models in simulation of single SPCs. The differences, capabilities and limitations of the three models are discussed based on the experimental data and the simulation results.

2. Experimental details

Sheets with thickness 1.2 mm of the aluminum alloy AA3103 in the fully annealed condition were investigated. Detailed information about chemical composition, grain size and crystallographic texture can be found in Zhang et al. (2014).

The experimental study consists of five test series. All tests are performed at room temperature with a deformation rate of about 10^{-2} s^{-1} . Stress-strain curves from the tension tests are presented in terms of the true (Cauchy) stress σ and the true (logarithmic) plastic strain ε_t^p . In sequences involving a SPC between two tension tests, the prestrain is measured as the true strain in the direction of the tensile prestrain. In order to quantify prestrains by rolling, the equivalent plastic strain was estimated by the von Mises strain, which is defined by

$$\bar{\varepsilon}_{VM} = \int \sqrt{\frac{2}{3} \mathbf{D}^p : \mathbf{D}^p} dt \quad (3)$$

The r-values (or Lankford coefficients) were calculated in the monotonic tensile tests according to the definition

$$r = \frac{d\varepsilon_w^p}{d\varepsilon_t^p} \quad (4)$$

where $d\varepsilon_w^p$ and $d\varepsilon_t^p$ are the true plastic strain increments in the width and thickness directions of the flat dog-bone shaped tensile sample. An average value of the r-value was calculated based on the results up to incipient diffuse necking.

Uniaxial tension tests were carried out on specimens taken from the as-received material along every 15° from the rolling direction (RD). The tensile samples had a gauge length of 50 mm and a width of 12.5 mm. The tests were conducted on a 500 kN MTS testing machine, using a clip-on extensometer to measure the longitudinal and transverse strains.

The Bauschinger effect was evaluated by performing compression-tension tests using small tensile samples that allowed pre-deformation in uniaxial compression without buckling. Samples with 4 mm gauge length and 3 mm width were machined parallel to the RD. The tests were conducted on a zwickiLine 2.5 kN testing machine for low-force testing, using a laser extensometer to measure the longitudinal strain. The specimen was directly gripped by the two crossheads of the machine. Since the samples were relatively short, the desired prestrains could be obtained in compression without applying any anti-buckling device. After a certain compression strain, the movement was stopped, the specimen unloaded and loaded in tensile mode. Compressive strains of 2% and 4% were reached without buckling.

SPCs between two subsequent tension tests were obtained by first performing tension tests along the RD on a large sample with gauge length 150 mm and width 75 mm, followed by tension tests on smaller samples (gauge length 7 mm and width 4 mm) machined from the pre-deformed one along every 15° from the RD, as illustrated in Fig. 1a. The large sample was tested on an MTS testing machine, while the small samples were tested on a zwickiLine testing machine. The large samples were prestrained to 8 % engineering strain and unloaded, after which the smaller samples were machined from the gauge region, see Fig. 1a. Digital Image Correlation (DIC) was used to check that the strain field in the gauge area of the large sample was uniform, as shown in Fig. 1b. The results show that the strain distribution in the gauge region of the large sample remained homogeneous and a uniaxial stress state was maintained in this area. The plastic strain of the large sample was measured by a clip-on extensometer. The extensometer was tightly fixed by rubber bands, which can be seen as the lines between the three red regions shown in Fig. 1b.

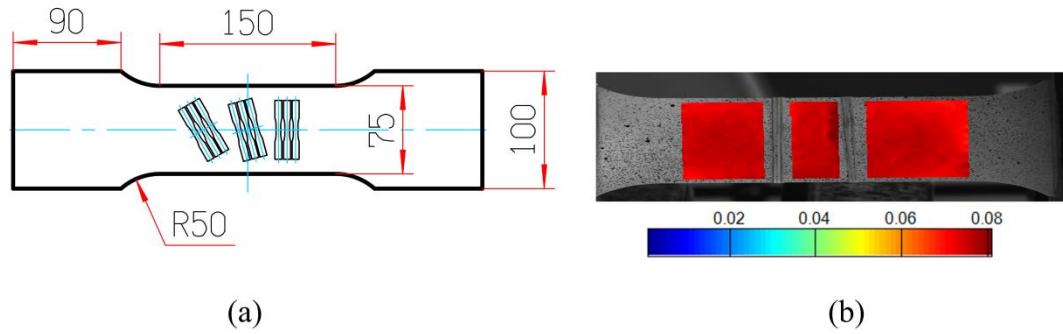


Fig. 1. Specimens used in the tension-tension tests: (a) large sample with small samples machined from the gauge region, and (b) strain maps in the gauge region of the large tensile sample evaluated at an engineering strain of 0.08. The equivalent von Mises strain $\bar{\epsilon}_{VM}$ is applied as a convenient measure of the two-dimensional strain field extracted by DIC.

SPCs were also obtained by pre-deformation by rolling along the transverse direction (TD). The AA3103 sheet metal was cut into square plates with dimensions 100 mm \times 80 mm, and these plates were rolled along the TD with a speed of 5 m/min in a 2 high rolling mill with roll diameter 205 mm. No lubricant was used. The thickness reductions were about 2%, 4%, 7%, 13% and 18%. During rolling without lubrication shear strains will occur towards the plate surface. However, with the considered roll gap geometry, a nearly plane strain deformation with only small shear strains towards the plate surface are expected, estimated following the work by Yang et al. (2010). Subsequently, uniaxial tensile samples with 7 mm gauge length and 4 mm width were machined along the RD and tension tests were carried out. These tension tests were conducted on the zwickiLine testing machine. Different rolling reductions were considered to evaluate the effect of the rolling process on the subsequent stress-strain behavior.

Three step tests containing two subsequent SPCs were obtained by a sequence of uniaxial tension in the RD, rolling along the TD and finally uniaxial tension along a given material direction. The large tensile sample, shown in Fig. 1a, was firstly pre-strained to 8 % engineering strain along the RD and unloaded. The gauge region of this sample was then rolled along the TD, as described above. Finally, small tensile samples with gauge length 7 mm and width 4 mm were machined from the stretched and rolled sheet. The final tension tests were performed along every 15° from the RD. As before, the large sample was tested on the MTS testing machine, while small samples were tested on the zwickiLine testing machine.

3. Constitutive models and calibration procedure

A detailed presentation of the MHH model can be found in Mánik et al. (2015). The QHH model is described in Qin et al. (2017a), whereas the version of the HAH model used in the current paper is presented in Qin et al. (2017b). In the current study, the non-quadratic, anisotropic Yld2000-2d yield function (Barlat et al., 2003) for plane stress conditions is used to describe the initial anisotropy of the AA3103 sheet in all the three models, combined with a two-term Voce rule (Voce, 1948) for accurate modeling of isotropic hardening.

The identification procedure for the HAH model is outlined in Barlat et al. (2014). For the MHH model, a similar calibration procedure as used by Mánik et al. (2015) is adopted to obtain the parameters. The parameter identification process of the QHH model is described in Qin et al. (2017a). A brief account of the calibration procedures is given in the following. Firstly, the coefficients of the Yld2000-2d yield function are identified by the use of the stress-strain curves from the uniaxial tension tests in the various tensile directions on the as-received material. Secondly, for the HAH model, the parameters of the isotropic hardening rule are fitted from the uniaxial tension stress-strain curves, whereas the parameters governing the plastic anisotropy after reverse SPCs are calibrated based on the stress-strain curves from the compression-tension tests. For the MHH and QHH models, the parameters of the isotropic and kinematic hardening rules are calibrated by using the stress-strain curves of the uniaxial tension tests and the compression-tension tests. Thirdly, the orthogonal hardening parameters of the three models are calibrated from the reloading curves in the tension-tension tests. The reloading curves from the rolling-tension tests are used to evaluate the credibility of the models.

4. Experimental results

The tensile test data presented in this study were obtained with samples of different sizes. To investigate if the sample size could influence the stress-strain response in tension, tests along the RD were conducted for the virgin material using all samples. The resulting stress-strain curves are shown in Fig. 2, and it is concluded that the sample size has no influence on the response in tension.

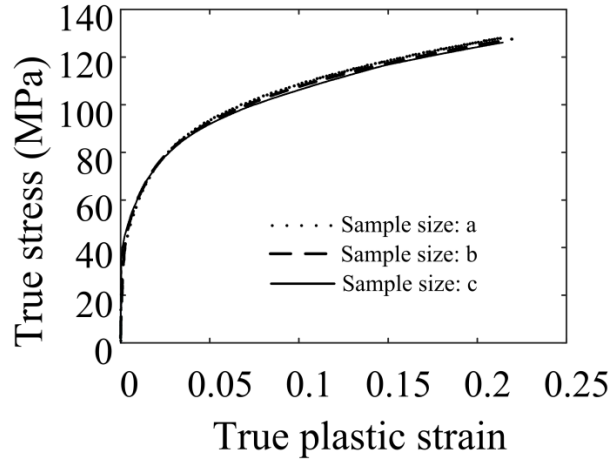


Fig. 2. True stress-strain curves from tension test along the RD with different sample sizes: (a) 50 mm gauge length and 12.5 mm width; (b) 4 mm gauge length and 3 mm width; (c) 7 mm gauge length and 4 mm width.

4.1 Monotonic uniaxial tension tests

The true stress-strain curves of the as-received material measured at every 15° from the RD are plotted in Fig. 3. To characterize the plastic anisotropy in strength, we apply the yield stress in each tensile direction divided by the yield stress in the RD at the same level of specific plastic work. The normalized yield stresses at a specific plastic work of 15 MPa and the r-values are shown in Table 1. It is found that the yield stress decreases monotonically with the angle from the RD, while the r-value has a maximum value around 30° to 45° from the RD.

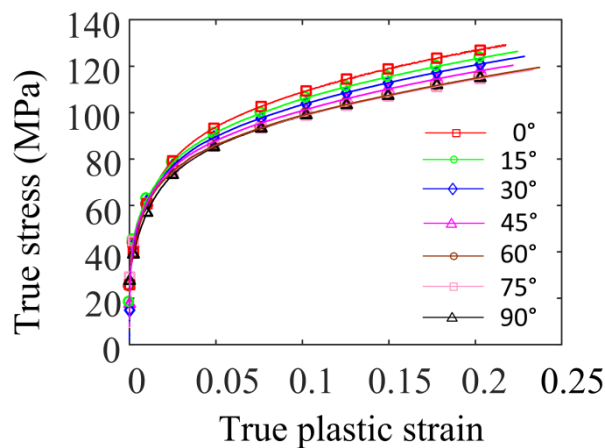


Fig. 3. True stress-strain curves from uniaxial tension tests along every 15° from the RD. All curves are plotted up to necking.

Table 1. Normalized yield stresses and r-values from monotonic tension tests.

Angle from RD	0°	15°	30°	45°	60°	75°	90°
Normalized yield stress	1	0.976	0.959	0.939	0.920	0.917	0.920
r-value	0.665	0.772	0.865	0.858	0.753	0.552	0.448

Using the experimental data from the tension tests in combination with the equi-biaxial yield stress ($\sigma_{11} = \sigma_{22}$) and equi-biaxial strain ratio, $r_b = d\varepsilon_{22}^p / d\varepsilon_{11}^p$, the plane-stress yield surface of the as-received material can be uniquely identified. It is assumed here that the x_1 axis is along the RD and the x_2 axis is along the TD. Since the equi-biaxial tensile test is difficult to perform with the desired accuracy, a polycrystal plasticity model (Van Houtte, 2005) was used to carry out a virtual equi-biaxial tension test based on the measured texture, see e.g. Zhang et al. (2014) for a detailed explanation. The normalized equi-biaxial yield stress was found to be 0.975, while r_b was determined to 1.127. Using the available experimental data in Table 1 and the results from the virtual equi-biaxial tension test, the eight anisotropy coefficients of the Yld2000-2d yield function were determined, see Table 2. The yield surface exponent m was set to 8, which is the default value for fcc materials like aluminum alloys.

Fig. 4 shows the experimental and fitted distributions of the normalized yield stress and the r-value for the AA3103 alloy. It is seen that the Yld2000-2d yield function gives a good representation of the variation of yield stress and plastic flow (as represented by the r-value) with tensile direction.

Table 2. Coefficients of the Yld2000-2d yield function.

α_1	α_2	α_3	α_4	α_5	α_6	α_7	α_8	m
0.950	1.026	0.941	1.089	1.037	1.085	1.059	1.127	8

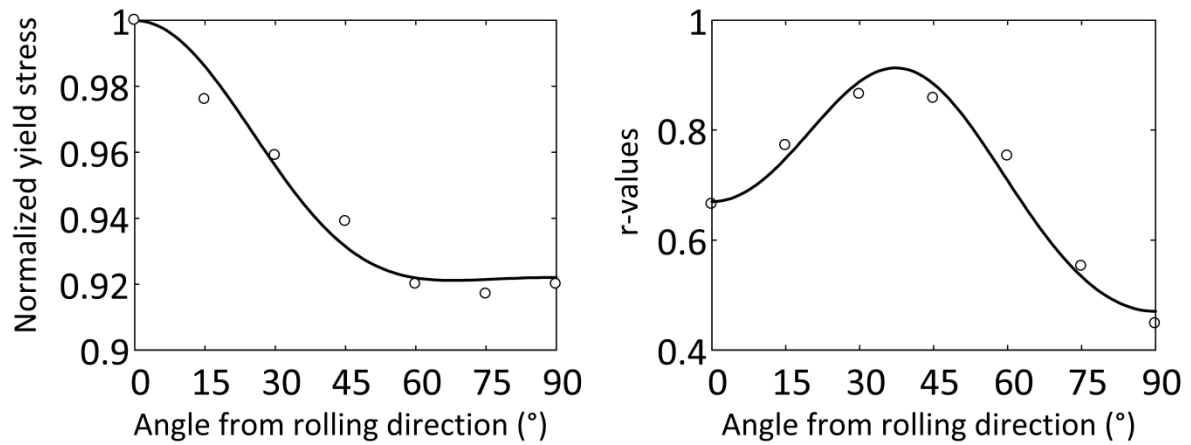


Fig. 4. Plastic anisotropy in terms of normalized yield stress and r-value as a function of the tensile angle from the RD based on the monotonic tension tests and the fitted Yld2000-2d yield function.

4.2 Compression-tension tests

The behavior of the material under reversed loading is evaluated from the compression-tension tests. Fig. 5 presents stress vs. accumulated strain for a tension test in the RD and for specimens pre-compressed to 2% and 4% along the RD. The results from three repeated tests are plotted for each prestrain level. The material exhibits a strong Bauschinger effect and hardening stagnation after the reverse SPC. The flow stress is significantly lower during reloading in tension subsequent to compression as compared to monotonic tension, but this difference diminishes with further straining. It is evident that the transient behavior lasts considerably longer for the largest prestrain. During the relatively long transient subsequent to the SPC, the curve gradually catches up with the monotonic curve, and the work hardening rate gradually increases. As a consequence, the onset of necking is delayed and the uniform elongation is increased for the pre-compressed material.

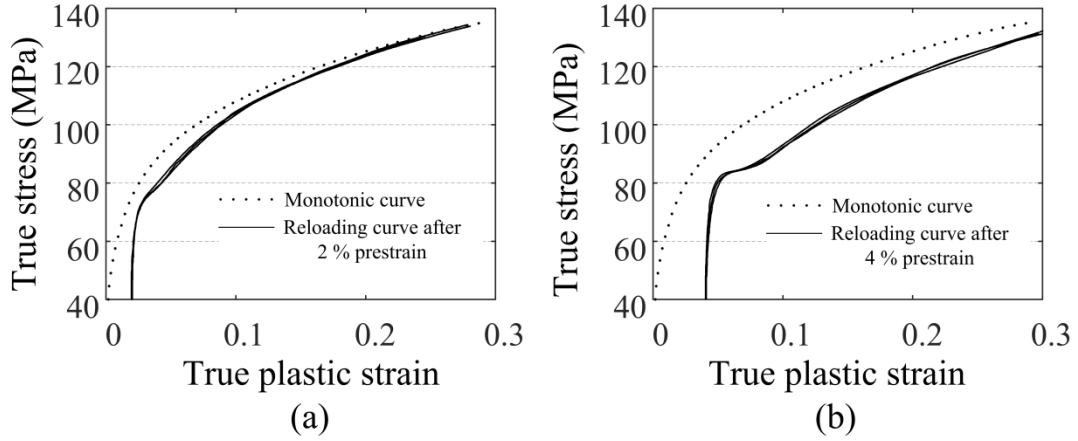


Fig. 5. True stress-strain curves in tension along the RD after prestraining in compression to (a) 2 % and (b) 4 % together with the stress-strain curve for monotonic tension. All curves are plotted up to necking.

4.3 Tension-tension tests and rolling-tension tests

The results of the tension-tension tests are presented in Fig. 6. In each sub-figure, the true stress-strain curves from the second tension step (i.e., after 8 % tensile prestrain in the RD) along every 15° from the RD are plotted up to necking (dashed lines). In addition, the monotonic stress-strain curve in the same direction as the second tension step is shown for comparison. Stress overshoot and slight permanent softening are observed in some of the reloading curves. The necking strain is nearly the same as for the as-received material for reloading in the 0°, 15°, 30° and 45° directions, while it is reduced for reloading in the 60°, 75° and 90° directions. Note that the results from the tension-rolling-tension tests are plotted in Fig. 6. These results will be discussed in Section 4.4.

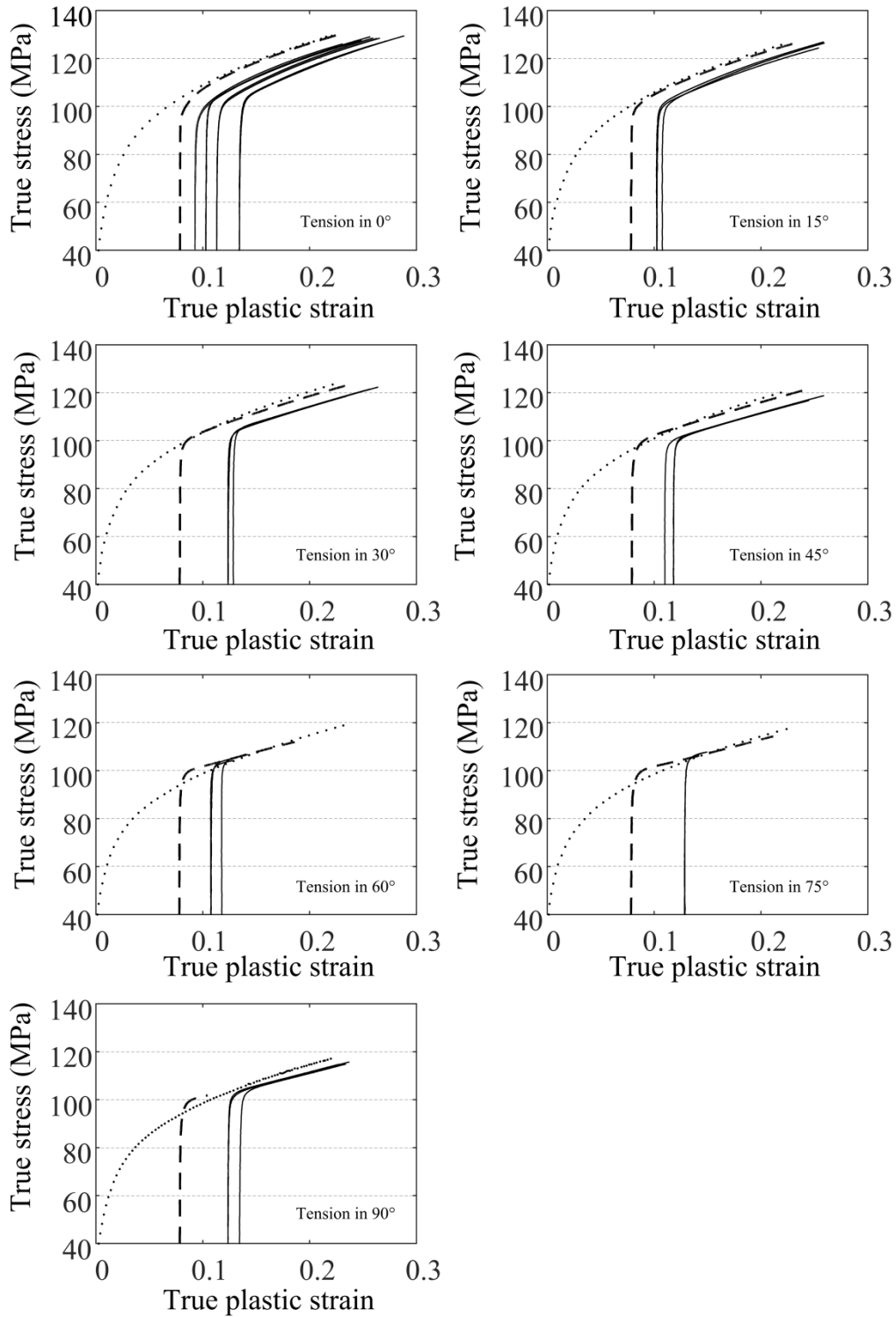


Fig. 6. True stress-strain curves in uniaxial tension along every 15° from the RD. Dotted lines represent the monotonic true stress-strain curve in the same direction as the reloading. Dashed lines represent tension tests with 8% pre-deformation in tension along the RD, while solid lines represent tension tests with a further pre-deformation step by rolling in the TD. All curves are plotted up to necking.

The results of the tension tests along the RD after prestraining by rolling in the TD are presented in Fig. 7. The true plastic prestrain by rolling was estimated by the von Mises strain. Alternatively, the prestrain could have been estimated as an equivalent strain based on a calibrated yield surface. However, this would add complexity, but only slightly change the results. The reloading yield stress is consistently lower than the unloading yield stress and the reduction increases with the prestrain. However, the reloading hardening rate converges toward that of the monotonic curve for all prestrains and the flow stress remains permanently lower than the monotonic tensile curve. Hardening stagnation is observed for the two largest prestrains by rolling.

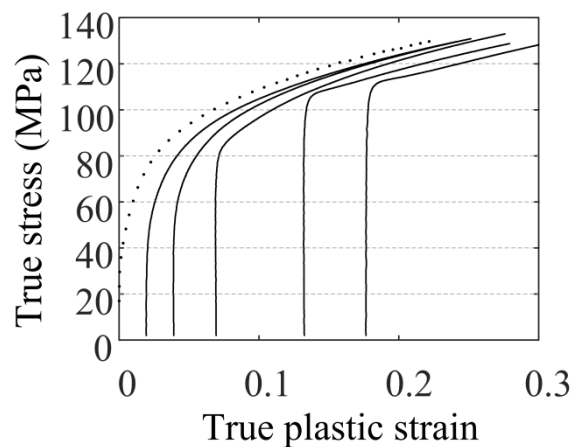


Fig. 7. True stress-strain curves in tension along the RD after rolling in the TD to various strain levels and corresponding monotonic stress-strain curve. The true plastic prestrain by rolling is estimated by the von Mises strain. All curves are plotted up to necking.

4.4 Tension-rolling-tension tests

To evaluate the stress-strain behavior after double SPCs, tension-rolling-tension tests sequences were performed. The tension test in the first strain path is along the RD, while the intermediate rolling in the second strain path is along the TD. The third strain path is tension along every 15° from the RD. The true stress-strain curves of the final tension tests are shown in Fig. 6, where the true prestrain from the second rolling step is estimated. Compared with the monotonic stress-strain curve, the reloading flow stress is markedly lower than the monotonic flow stress in the 0° , 15° , 30° and 45° directions, while the difference is less in the 60° , 75° and 90° directions. In these directions, the reloading curves of the tension-rolling-tension tests coalesce with those of the tension-tension tests, i.e., the plastic strain accumulated during the intermediate rolling appears not to affect the subsequent stress-strain behavior. For the double

SPCs with the third loading path along 0° , the permanent softening induced by intermediate rolling increases with increased pre-deformation by rolling in the second step.

5. Evaluation of constitutive models

In this section, stress-strain curves during proportional loading and after single SPCs of the AA3103 alloy are used to evaluate the capability of the three advanced plasticity models (namely the MHH, QHH and HAH models). The stress-strain curves from the experiments are presented in terms of the true stress σ and true (or logarithmic) plastic strain ε_l^p in uniaxial tension. Pure experimental prestrains are commonly quantified as von Mises strains. However, when comparing the influence of the prestrains in model predictions, the convenient choice is rather to consider the equivalent strain, as defined by the model. Unfortunately, this cannot be expressed explicitly in the complex models applied here, but is calculated by running the models numerically. Prestrains calculated by the models depend on each model calibration of the yield surface and the kinematic hardening. However, in the cases considered here, the differences between the calculated true plastic (equivalent) prestrains by the three models are very small, less than 0.03%. Hence, in the following figures, the true plastic prestrain in the tensile direction calculated by the HAH model will be used for plotting the experimental results. Note that the model-based prestrains in this section are slightly different from the logarithmic or von Mises strains used to present the experimental curves in Fig. 6.

The identified parameters of the three models are listed in Table 3. We refer to Mánik et al. (2015) and Qin et al. (2017a, 2017b) for a detailed description of the three models and the associated parameters.

Table 3. Model parameters for AA3103 alloy.

MHH model																
m	R_0	R_1^{sat}	$\Delta\epsilon_{R_1}$	R_2^{sat}	$\Delta\epsilon_{R_2}$	X_1^{sat}	$\Delta\epsilon_{X_1}$	X_2^{sat}	$\Delta\epsilon_{X_2}$	$\Delta\epsilon_P$	$\Delta\epsilon_o$	$\Delta\epsilon_r$	q_0	q_r	k_0	k_r
[-]	[MPa]	[MPa]	[-]	[MPa]	[-]	[MPa]	[-]	[MPa]	[-]	[-]	[-]	[-]	[-]	[-]	[MPa]	[MPa]
8	42.10	44.10	0.198	22.86	0.018	28.6	0.198	15.24	0.018	0.06	0.0012	0.0075	0.16	0.9	50	1000
QHH model																
m	R_0	R_1^{sat}	$\Delta\epsilon_{R_1}$	R_2^{sat}	$\Delta\epsilon_{R_2}$	X_1^{sat}	$\Delta\epsilon_{X_1}$	X_2^{sat}	$\Delta\epsilon_{X_2}$	$\Delta\epsilon_P$	$\Delta\epsilon_o$					
[-]	[MPa]	[MPa]	[-]	[MPa]	[-]	[MPa]	[-]	[MPa]	[-]	[-]	[-]					
8	42.10	44.10	0.198	22.86	0.018	29.40	0.198	15.24	0.018	0.06	0.0012					
$\Delta\epsilon_r$	q_0	q_r	k_0	k_r	α	n	q									
[-]	[-]	[-]	[MPa]	[MPa]	[-]	[-]	[-]									
0.0075	0.24	0.9	50	1000	0.8	1	2									
HAH model																
m	q	R_0	R_1^{sat}	$\Delta\epsilon_{R_1}$	R_2^{sat}	$\Delta\epsilon_{R_2}$	k_1	k_2	k_3	k_4	k_5					
[-]	[-]	[MPa]	[MPa]	[-]	[MPa]	[-]	[-]	[-]	[-]	[-]	[-]					
8	8	42.1	73.5	0.198	38.1	0.018	20	50	0.95	0.6	2.75					
k_6	k_7	k_o	k_L	L	k_S	S	k	z	k_R	k'_R						
[-]	[-]	[-]	[-]	[-]	[-]	[-]	[-]	[-]	[-]	[-]						
1.5	300	30	165	1.1	0	0	25	5	15	0.20						

5.1 Calibration tests

The simulated stress-strain curves after reverse SPCs are compared with the experimental data in Fig. 8. Both the MHH and QHH models use non-linear kinematic hardening with equal description of the Bauschinger effect, the hardening stagnation and the permanent softening after reverse SPCs. Hence, the two models give identical results in the simulation of the compression-tension test, as shown in Fig. 8. It is found that all three models capture the transient behavior after reverse SPCs with reasonably accuracy. For the 2% prestrain, the reloading hardening rate of the HAH model is higher and slightly closer to the experiments than the MHH and QHH models, whereas the MHH and QHH models give a better description of the stress inflexion of reloading curve after 4% prestrain.

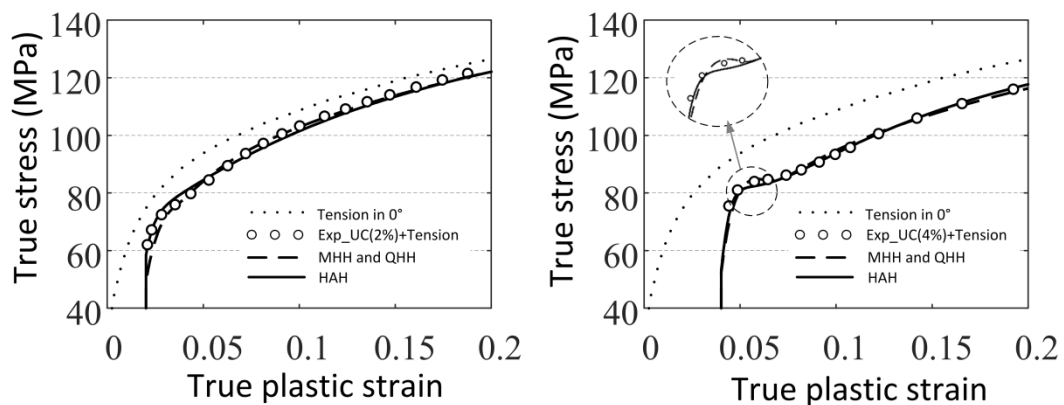


Fig. 8. Comparison of the simulated and experimental stress–strain curves from tension tests prestrained by compression (2% and 4%) together with the monotonic loading curve.

The experimental and simulated stress-strain curves at every 15° from the RD after 8% tensile prestrain along the RD are presented in Fig. 9. In each figure, the monotonic loading curve (dotted line) from experiments is plotted along with the experimental reloading curve (circles) in the same direction. In the 0° direction, the simulated reloading curves are on top of the monotonic loading curve from the experiment, while the experimental reloading curve exhibits a transient. The three models give similar results for reloading in the 15° and 30° directions, and these results are in reasonable agreement with the experiments. In the remaining directions, the MHH and QHH models give similar results but significantly underestimate the experimental reloading curve. The HAH model is rather accurate in the first phase after the SPC but then it deviates from the experimental reloading curves and converges toward the

same stress level as the two other models. The origin of this softening behavior is the way the HAH model distorts the reversal part of the yield surface to capture the Bauschinger effect. The exponent q was increased from 2 to 8 to obtain an optimal calibration of the HAH model and thus capture the first phase of the reloading curves.

5.2 Rolling-tension tests

The rolling-tension test data was not used in the calibration of the models but is used to evaluate the predictive capability of the models. The experimental and simulated stress-strain curves in tension along the RD after prestraining by rolling along the TD are presented in Fig. 10 together with the monotonic loading curves in the RD from the experiments. The permanent softening is captured by the MHH and QHH models, but the stress level in the first phase after the SPC is higher than in the experiments for the two lowest prestrains. A spurious transient behavior is predicted by the MHH model for the two highest prestrains, while the QHH model is in good agreement with the experiments. The stress level predicted by the HAH model is too high for all prestrains, and the predicted behavior is characterized by a weak stress overshoot and slight permanent softening.

Based on these comparisons, neither of the three plasticity models could reproduce the tension–tension tests in a satisfactory manner, nor could they capture the qualitative differences between tension-tension and rolling-tension tests performed with comparable Schmitt angles. As a result of this conclusion, simulations of the double SPC experiments were not conducted.

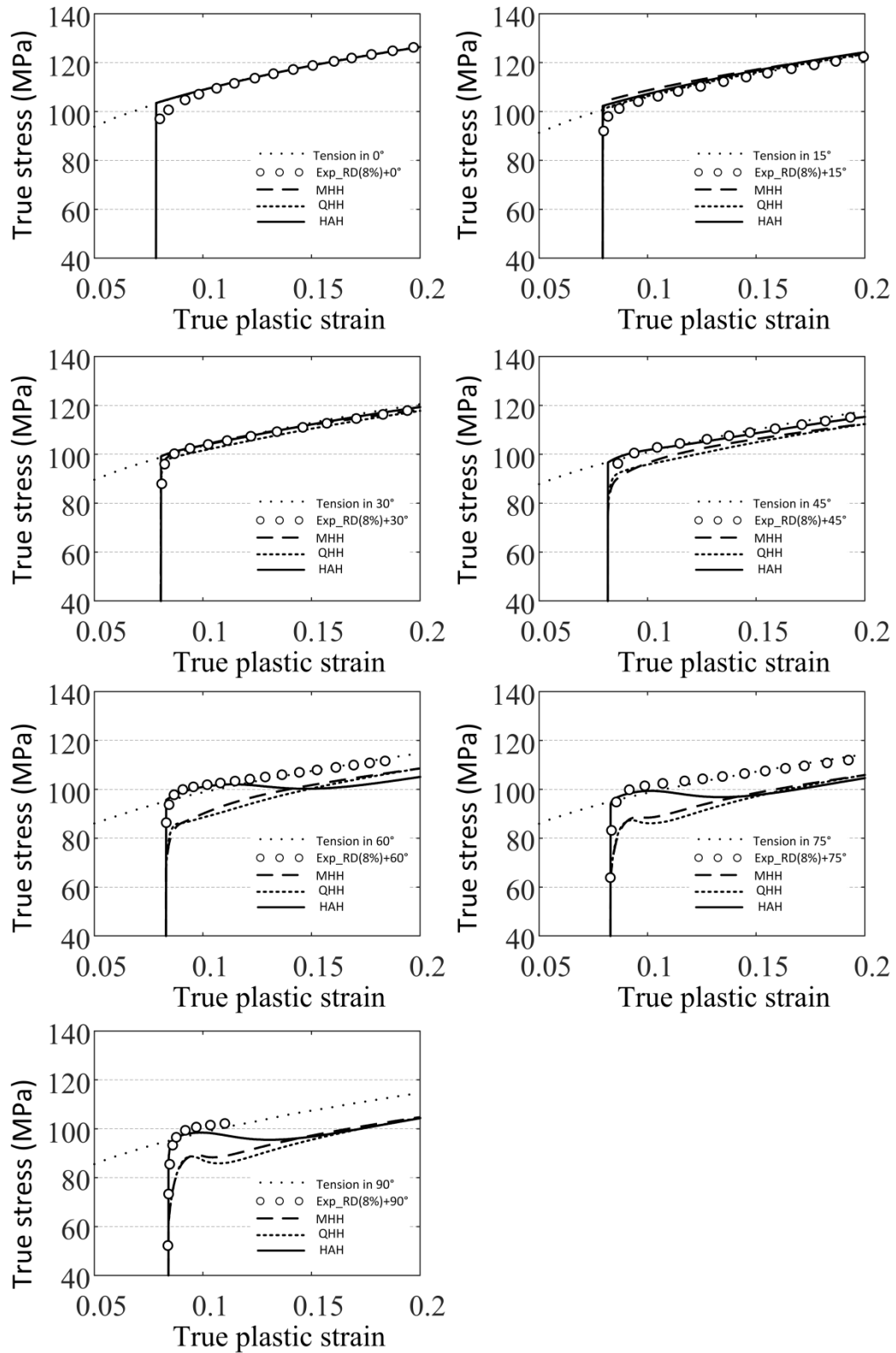


Fig. 9. Experimental and simulated stress-strain curves in uniaxial tension at every 15° from the RD after 8% prestrain by uniaxial tension test in the RD and corresponding monotonic loading curve.

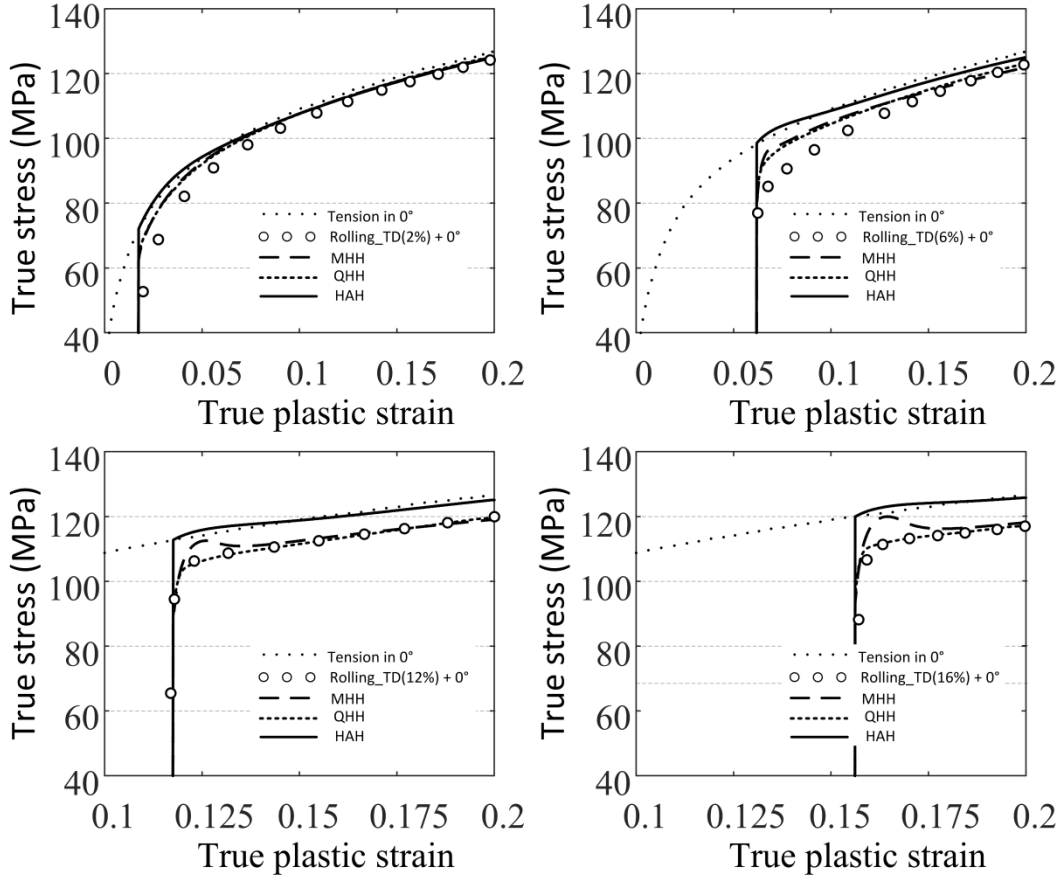


Fig. 10. True stress-strain curves in tension along the RD after rolling in the TD to various strain levels and corresponding monotonic stress-strain curve.

6. Discussion

In the work by Holmedal et al. (2008) on a similar alloy, permanent softening was observed after orthogonal SPCs, i.e., with Schmitt angle equal to 90° . In commercially pure aluminum with random grain orientations, Mánik et al. (2015) carefully measured a similar behavior, which correlated with the measured Bauschinger effect. Hence, the phenomenon was well captured by including a kinematic hardening model. Also for the alloy considered here, the magnitude of the cross-softening correlates well with the measured Baschinger effect, but then only for case of pre-deformation by rolling. When the orthogonal pre-deformation was produced by a tensile test, no permanent softening was measured. This challenges the idea that the cross-hardening effect depends solely on the Schmitt factor, and also our current understanding and its implementation into mathematical models.

Stress overshoot is observed in the reloading curves of the tension-tension tests for $\alpha \in [30^\circ, 90^\circ]$. As a measure of the amount of cross-hardening, the maximum ratio of the peak flow stress after the SPC (when it exists) and the flow stress in monotonic tension at the same true plastic strain is adopted. The measured maximum stress ratio is shown in Fig. 11 as a function of the angle from the RD. In the experimental data, the reloading curve for $\alpha = 60^\circ$ exhibits the highest stress overshoot, amounting to about 4 % of the flow stress in monotonic tension. This is similar to, but smaller in magnitude than, results for commercially pure aluminum (Mánik et al., 2015), where a stress overshoot of about 6% was found in orthogonal rolling-tension tests with a comparable amount of prestrain. As compared to the AA3103 alloy, the Bauschinger effect of this commercial pure aluminum was small. The AA3103 alloy is similar to the commercial pure aluminum, except that it has additional 1 wt% manganese. Some of the manganese atoms are in solid solution and the rest are tied up in particles (dispersoids) formed during the homogenization heat treatment. It is known that the dispersoids may cause a strong Bauschinger effect (Zhao et al., 2013). It is reasonable to assume that the Bauschinger effect contributes also to weaken the stress overshoot at Schmitt angles smaller than 180° . In crystal plasticity simulations some of the slip systems are reversed, even at orthogonal SPCs, such as for a tension test in the RD with pre-rolling in the TD or for the tension-tension test with $\alpha \approx 60^\circ$. Hence, if one assumes that the Bauschinger effect to some extent acts individually on the slip systems, a correlation between the Bauschinger effect and the cross hardening can be expected for materials with a strong Bauschinger effect. Furthermore, the number of reversed slip systems depends on the texture and on the deformation modes in the first and second strain paths, hence a simple correlation with the Schmitt angle may not exist.

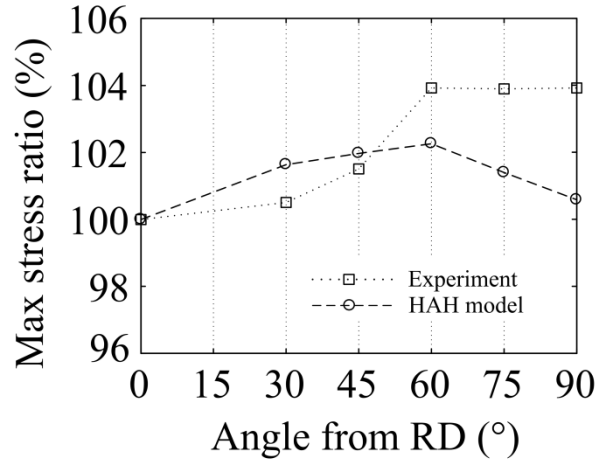


Fig. 11. Experimental and simulated (with the HAH model) maximum stress ratio for tension-tension tests at various angles from the RD.

In general, a strong Bauschinger effect may either be due to the composite effect, which would be the case for a two-phase material or a material with a large volume fraction of strong particles, or it may be due to the reversibility and polarization of dislocation structures. In the AA3103 alloy, both mechanisms are present due to the particles (i.e., the dispersoids), but the main contribution is related to the reversibility of dislocation loops and structures formed around the dispersoids (Zhao et al., 2013). Hence, one may expect the cross-hardening to depend on the number of slip systems that are reversed subsequent to the SPC, which is determined by the deformation mode (i.e., tension or rolling) and on the grain orientations (i.e., the crystallographic texture). It is noted that Holmedal et al. (2008) reported a strong cross-hardening for a similar AA3103 alloy, even stronger than the pure metal behavior with a maximum stress ratio of 8% at a comparable prestrain. However, as discussed in Zhao et al. (2013), the number density of dispersoids depends strongly on the homogenization treatment, which was not specified in Holmedal et al. (2008), but this work clearly shows that one should expect an equally strong cross-hardening effect in the AA3103 alloy as in commercial pure aluminum.

It is interesting to note the qualitatively different behavior between the tension-tension tests with $\alpha = 60^\circ$ in Fig. 6 and the rolling-tension tests in Fig. 7, even though the Schmitt angle is very similar in these two tests. The cross-hardening is not absent in the rolling-tension tests, but it is overshadowed by another mechanism involving a lower initial yield stress and an increased hardening rate. In particular, the hardening rate is large for small prestrains. The cross-hardening in the rolling-tension and tension-tension tests can be clearly seen from the

characteristic dip in the Kocks-Mecking diagram presented in Fig. 12. In the figure, the two rolling prestrains are slightly larger than the tensile prestrain. The rolling-tension tests effectively have weaker stress overshoot, in particular at small prestrains, and they reveal significantly more permanent softening. Thus, the assumption that the SPC behavior correlates mainly with the Schmitt angle of the SPC is obviously incorrect for the AA3103 alloy. More complex relations between the strain modes before and after the SPC have to be considered and the influence of texture and slip system activation may play an important role.

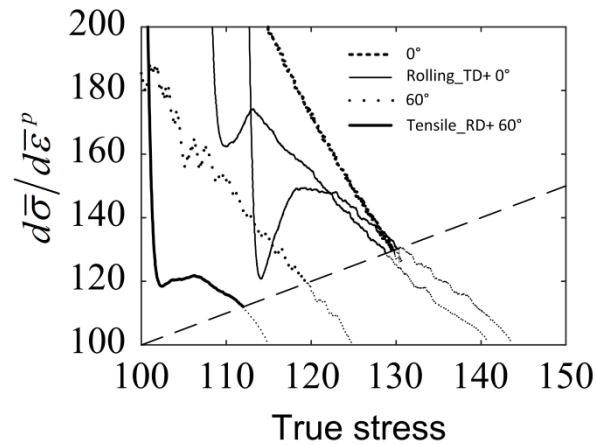


Fig. 12. Kocks-Mecking plots for tension in the 60° direction with and without 8 % prestrain in tension along the RD and for tension along the RD with and without 12 % and 15 % prestrain by rolling in the TD.

The permanent softening caused by the rolling prestrain can be quantified by the ratio between the flow stress after the SPC and the flow stress during monotonic straining at the same true plastic strain. This stress ratio at a true plastic strain of 0.2 is plotted in Fig. 13 as a function of the rolling prestrain. Results from the rolling-tension tests and the tension-rolling-tension tests are shown. It is evident that the permanent softening increases nearly linearly with the rolling prestrain. However, the effect of the rolling prestrain is stronger for the double SPC, which involves two orthogonal SPCs in terms of the Schmitt factor, i.e., first from tension to rolling, then back from rolling to tension. It is therefore reasonable to assume that both the SPCs involved in the tension-rolling-tension tests contribute to the subsequent permanent softening.

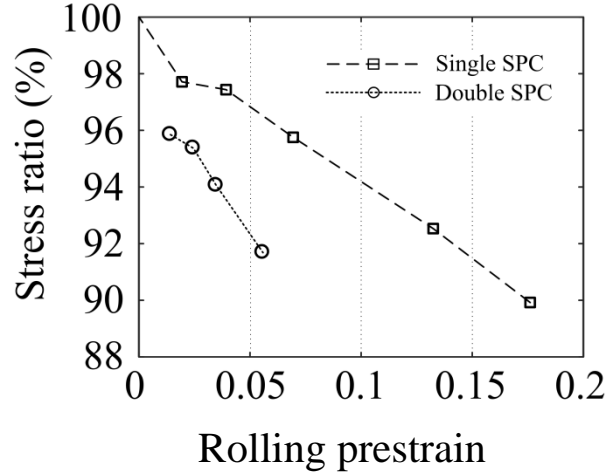


Fig. 13. Stress ratio versus rolling prestrain at a total true plastic strain of 0.2 showing the degree of permanent softening. Results based on the rolling-tension tests in Fig. 7 and the tension-rolling tension tests in Fig. 6 are shown.

It has earlier been reported that all the three advanced plasticity models considered here are capable of describing a strong Bauschinger effect or a considerable cross-hardening effect (Barlat et al., 2014; Mánik et al., 2015; Qin et al., 2017b). In the current work, a material is investigated for which both effects are strong. In all the three models, a strong Bauschinger effect will influence the cross-hardening effect after the SPC, but in various ways by either distortion of the yield surface in the HAH model or by translation of the yield surface (i.e., kinematic hardening) in the QHH and MHH models.

From Fig. 9 and Fig. 11 it is seen that the HAH model can describe the stress overshoot that occurs immediately after the SPC in the tension-tension tests, but then fails to predict the remaining part of the stress-strain curve. In Fig. 9, a dramatic change in the behavior predicted by the HAH model is observed when α is changed from 45° to 60° . The main difference between these two stress-strain curves is that the stress-based Schmitt angle adopted in the HAH model is lower than 90° for $\alpha = 45^\circ$ and larger for $\alpha = 60^\circ$. In the HAH model, the direction of the rotation of the microstructure deviator (see e.g. Qin et al. (2017b)) is opposite if the Schmitt angle is lower versus higher than 90° . This gives rise to a mathematical singularity in the HAH model, which induces the observed softening behavior only when the Schmitt angle is larger than exactly 90° . Thus, the predicted stress-strain curve after a tension-tension SPC with an infinitesimally smaller Schmitt angle than 90° behaves significantly different. Prestraining by rolling in the TD followed by tension in the RD, as in Fig. 10, gives a Schmitt angle exactly equal to 90° , which in the HAH model is treated as Schmitt angles less

than 90° . Hence, the permanent softening is completely lacking in the simulations of rolling-tension tests with the HAH model, and the experimentally observed permanent softening in these tests cannot be reproduced. A more detailed explanation of the mathematical weakness and reason for this spurious work hardening behavior of the HAH behavior can be found in Qin et al., (2017b).

The kinematic hardening in the MHH and QHH models is applied primarily to describe the Bauschinger effect in pure strain reversal tests. However, a reduction of the yield stress subsequent to other SPCs will occur as a consequence of the translation of the yield surface, by a gradually increased amount as the Schmitt angle increases from 0° toward 180° . In contrast, the transient isotropic expansion of the yield surface after an orthogonal SPC, governed by the parameter S_o that models cross-hardening effects, is gradually reduced as the Schmitt angle decreases/increases from 90° toward $0^\circ/180^\circ$. In the tension-tension tests in Fig. 6, the cross-hardening contribution will reach a maximum value near $\alpha = 60^\circ$, which approximately corresponds to a Schmitt angle of 90° , whereas the stress reduction induced by the kinematic hardening will be strongest at $\alpha = 90^\circ$. Hence, it is not possible to make the cross-hardening compensate the stress reduction due to kinematic hardening correctly at all angles.

It is interesting to note that the QHH model provides a reasonably good description of the rolling-tension experiments in Fig. 10, even though these experiments were not part of the calibration. The experimentally observed permanent softening in these stress-strain curves basically corresponds to the amount arriving from the kinematic hardening terms in the QHH model and the corresponding calibration to the strain reversal tests.

The microstructure deviator in the MHH model is defined in strain rate space, Mánik et al. (2015), while it is defined in the deviatoric stress space in the QHH model, Qin et al. (2017a). The evolution of the microstructure deviator depends on the attractor, which is defined by the current loading path. The evolution depends on the Schmitt factor, either $\cos \phi_D$ or $\cos \phi_\sigma$, which is based on the angle between the plastic strain rate tensor or the deviatoric stress tensor and the one memorized by the microstructure deviator. For the tension-tension tests in Fig. 9, the reloading curves predicted by the two models are nearly the same. However, in Fig. 10, for the reloading curves of the rolling-tension tests, a fictitious transient stress overshoot is predicted by the MHH model. The explanation is that the r-value of the tension test in the RD instantly after the pre-rolling in the TD has a high value that decreases rapidly, as reported by Mánik et al. (2015). Since the microstructure deviator applied in the MHH model to memorize

the deformation history is based on the plastic strain rate tensor, the Schmitt angle will be larger than 90° immediately after the orthogonal SPC and then start decaying rapidly toward smaller angles. The MHH model includes a contribution, controlled by the parameter S_r , that isotropically expands and then shrinks the yield surface after a strain reversal to model hardening stagnation. Because the Schmitt angle is temporarily larger than 90° after the orthogonal SPC, this contribution is activated and leads to the behavior seen in Fig. 10. In contrast, this contribution is important in the strain reversal tests in order to describe the inflexion point seen in the stress-strain curves in Fig. 8.

7. Conclusions

The stress-strain response of the aluminum alloy AA3103 after SPCs was investigated experimentally and attempted modeled by three advanced plasticity models. The strong Bauschinger effect found experimentally for the AA3103 alloy in strain reversal tests (compression-tension) included an inflexion point of the stress-strain curve and hardening stagnation, similar to previous findings for commercially pure aluminum. Cross hardening was observed after orthogonal strain-path changes in the tension-tension tests, whereas cross-softening was found after orthogonal strain-path change in the rolling-tension tests. Both cases resulted in permanent softening. It is suggested that the cross-hardening effect is influenced by the same mechanism that gives a strong Bauschinger, and for a given Schmitt angle, this interaction is stronger with prestraining by rolling than by tension. Hence, the response following a strain-path change is not only governed by the Schmitt angle, but also the more complex differences between the rolling and tensile deformation modes involved in the strain-path change. This interaction was even stronger during the double strain-path changes in the tension-rolling-tension tests.

The three advanced plasticity models, namely the MHH, QHH and the HAH models, were shown to describe the stress-strain response after reverse strain-path changes (compression-tension tests) with reasonably accuracy, but they all failed to give a satisfactory description of the cross hardening. The main reason is that all three models are based on an assumed correlation between the strain-path change and the Schmitt angle. Furthermore, the HAH model has a singularity in the work-hardening behavior that was clearly exposed during modeling attempts of the orthogonal strain-path changes.

The bottom line is that the hardening transients after strain-path changes in the considered AA3103 alloy are not solely controlled by the Schmitt factor. More complex ideas and models are required to describe loading cases where both the Bauschinger effect and the effects of orthogonal strain-path changes are strong.

Funding:

This research did not receive any specific grant from funding agencies in the public, commercial, or not-for-profit sectors.

Reference

- Banabic, D., Balan, T., Comsa, D., 2000. Yield criterion for orthotropic sheet metals. 8 th Int. Conf. Met. Form. 755–761.
- Barlat, F., Aretz, H., Yoon, J.W., Karabin, M.E., Brem, J.C., Dick, R.E., 2005. Linear transformation-based anisotropic yield functions. *Int. J. Plast.* 21, 1009–1039.
- Barlat, F., Brem, J.C., Yoon, J.W., Chung, K., Dick, R.E., Lege, D.J., Pourboghrat, F., Choi, S.H., Chu, E., 2003. Plane stress yield function for aluminum alloy sheets - Part 1: Theory. *Int. J. Plast.* 19, 1297–1319.
- Barlat, F., Gracio, J.J., Lee, M.-G., Rauch, E.F., Vincze, G., 2011. An alternative to kinematic hardening in classical plasticity. *Int. J. Plast.* 27, 1309–1327.
- Barlat, F., Ha, J., Grácio, J.J., Lee, M.-G., Rauch, E.F., Vincze, G., 2013. Extension of homogeneous anisotropic hardening model to cross-loading with latent effects. *Int. J. Plast.* 46, 130–142.
- Barlat, F., Lian, K., 1989. Plastic behavior and stretchability of sheet metals. Part I: A yield function for orthotropic sheets under plane stress conditions. *Int. J. Plast.* 5, 51–66.
- Barlat, F., Vincze, G., Grácio, J.J., Lee, M.-G., Rauch, E.F., Tomé, C.N., 2014. Enhancements of homogenous anisotropic hardening model and application to mild and dual-phase steels. *Int. J. Plast.* 58, 201–218.
- Bauschinger, J., 1881. Changes of the elastic limit and the modulus of elasticity on various metals. *Zivilingenieur* 27, 289–348.
- Boger, R.K.K., Wagoner, R.H.H., Barlat, F., Lee, M.G.G., Chung, K., 2005. Continuous, large strain, tension/compression testing of sheet material. *Int. J. Plast.* 21, 2319–2343.
- Cao, J., Lee, W., Cheng, H.S., Seniw, M., Wang, H.-P., Chung, K., 2009. Experimental and numerical investigation of combined isotropic-kinematic hardening behavior of sheet metals. *Int. J. Plast.* 25, 942–972.
- Ha, J., Lee, M.-G., Barlat, F., 2013. Strain hardening response and modeling of EDDQ and DP780 steel sheet under non-linear strain path. *Mech. Mater.* 64, 11–26.
- Hershey, A. V, 1954. The plasticity of an isotropic aggregate of anisotropic face-centered cubic crystals. *J. Appl. Mech. Asme.* 21, 241–249.
- Hill, R., 1948. A Theory of the Yielding and Plastic Flow of Anisotropic Metals. *Proc. R. Soc. London A Math. Phys. Eng. Sci.* 193, 281–297.
- Holmedal, B., Van Houtte, P., An, Y., 2008. A crystal plasticity model for strain-path changes in metals. *Int. J. Plast.* 24, 1360–1379.
- Khan, A.S., Pandey, A., Stoughton, T., 2010. Evolution of subsequent yield surfaces and elastic constants with finite plastic deformation. Part II: A very high work hardening aluminum alloy (annealed 1100 Al). *Int. J. Plast.* 26, 1421–1431.
- Lee, J.-W., Lee, M.-G., Barlat, F., 2012. Finite element modeling using homogeneous anisotropic hardening and application to spring-back prediction. *Int. J. Plast.* 29, 13–41.

- Levkovitch, V., Svendsen, B., 2007. Accurate hardening modeling as basis for the realistic simulation of sheet forming processes with complex strain-path changes, in: 10th ESAFORM Conference on Material Forming. AIP Publishing, pp. 358–363.
- Liao, J., Sousa, J.A., Lopes, A.B., Xue, X., Pereira, A.B., 2017. Mechanical, microstructural behaviour and modelling of dual phase steels under complex deformation paths. *Int. J. Plast.* 93, 269–290.
- Lubliner, J., 2008. *Plasticity theory*. Courier Corporation, North Chelmsford, MA.
- Mánik, T., Holmedal, B., Hopperstad, O.S., 2015. Strain-path change induced transients in flow stress, work hardening and r-values in aluminum. *Int. J. Plast.* 69, 1–20.
- Peeters, B., Bacroix, B., Teodosiu, C., Van Houtte, P., Aernoudt, E., 2001a. Work-hardening/softening behaviour of b.c.c. polycrystals during changing strain:: Part II. TEM observations of dislocation sheets in an IF steel during two-stage strain paths and their representation in terms of dislocation densities. *Acta Mater.* 49, 1621–1632.
- Peeters, B., Kalidindi, S.R., Teodosiu, C., Houtte, P. Van, Aernoudt, E., 2002. A theoretical investigation of the influence of dislocation sheets on evolution of yield surfaces in single-phase B.C.C. polycrystals. *J. Mech. Phys. Solids.* 50, 783–807.
- Peeters, B., Seefeldt, M., Teodosiu, C., Kalidindi, S.R., Van Houtte, P., Aernoudt, E., 2001b. Work-hardening/softening behaviour of b.c.c. polycrystals during changing strain paths: I. An integrated model based on substructure and texture evolution, and its prediction of the stress–strain behaviour of an IF steel during two-stage strain paths. *Acta Mater.* 49, 1607–1619.
- Qin, J., Holmedal, B., Hopperstad, O.S., 2017a. A combined isotropic, kinematic and distortional hardening model for aluminum and steels under complex strain-path changes. *Int. J. Plast.* 101, 156–169.
- Qin, J., Holmedal, B., Zhang, K., Hopperstad, O.S., 2017b. Modeling strain-path changes in aluminum and steel. *Int. J. Solids Struct.* 117, 123–136.
- Satheesh Kumar, S.S., Raghu, T., 2015. Strain path effects on microstructural evolution and mechanical behaviour of constrained groove pressed aluminium sheets. *Mater. Des.* 88, 799–809.
- Schmitt, J.H., Shen, E.L., Raphanel, J.L., 1994. A parameter for measuring the magnitude of a change of strain path: Validation and comparison with experiments on low carbon steel. *Int. J. Plast.* 10, 535–551.
- Teodosiu, C., Hu, Z., 1995. Evolution of the intragranular microstructure at moderate and large strains: modelling and computational significance, in: *Proc. Numiform.* pp. 173–182.
- Tresca, H., 1864. Memoir on the flow of solid bodies under strong pressure. *Comptes-rendus l'académie des Sci.* 59, 754.
- Van Houtte, P., 2005. Deformation texture prediction: from the Taylor model to the advanced Lamel model. *Int. J. Plast.* 21, 589–624.
- Vincze, G., Barlat, F., Rauch, E.F., Tomé, C.N., Butuc, M.C., Grácio, J.J., 2013. Experiments

- and modeling of low carbon steel sheet subjected to double strain path changes. *Metall. Mater. Trans. A* 44, 4475–4479.
- Voce, E., 1948. The relationship between stress and strain for homogeneous deformation. *J Inst Met.* 74, 537–562.
- Von Mises, R., 1913. *Mechanik der Festen Körper im Plastisch-Deformablen Zustand.* Nachrichten von der K. Gesellschaft der Wissenschaften zu Göttingen, Math. Klasse 582.
- Yang, H.P., Sha, Y.H., Zhang, F., Zuo, L., 2010. Through-thickness shear strain control in cold rolled silicon steel by the coupling effect of roll gap geometry and friction. *J. Mater. Process. Technol.* 210, 1545–1550.
- Yoshida, F., Uemori, T., Fujiwara, K., 2002. Elastic–plastic behavior of steel sheets under in-plane cyclic tension–compression at large strain. *Int. J. Plast.* 18, 633–659.
- Yoshida, K., Tsuchimoto, T., 2018. Plastic flow of thin-walled tubes under nonlinear tension-torsion loading paths and an improved pseudo-corner model. *Int. J. Plast.* 114, 214–229.
- Zhang, K., Holmedal, B., Hopperstad, O.S., Dumoulin, S., 2014. Modelling the plastic anisotropy of aluminum alloy 3103 sheets by polycrystal plasticity. *Model. Simul. Mater. Sci. Eng.* 22, 075015.
- Zhao, Q., Holmedal, B., 2013. Modelling work hardening of aluminium alloys containing dispersoids. *Philos. Mag.* 93, 3142–3153.
- Zhao, Q., Holmedal, B., Li, Y., 2013. Influence of dispersoids on microstructure evolution and work hardening of aluminium alloys during tension and cold rolling. *Philos. Mag.* 93, 2995–3011.

Figure Captions:

Fig. 1. Specimens used in the tension-tension tests: (a) large sample with small samples machined from the gauge region, and (b) strain maps in the gauge region of the large tensile sample evaluated at an engineering strain of 0.08. The equivalent von Mises strain $\bar{\epsilon}_{VM}$ is applied as a convenient measure of the two-dimensional strain field extracted by DIC.

Fig. 2. True stress-strain curves from tension test along the RD with different sample sizes: (a) 50 mm gauge length and 12.5 mm width; (b) 4 mm gauge length and 3 mm width; (c) 7 mm gauge length and 4 mm width.

Fig. 3. True stress-strain curves from uniaxial tension tests along every 15° from the RD. All curves are plotted up to necking.

Fig. 4. Plastic anisotropy in terms of normalized yield stress and r-value as a function of the tensile angle from the RD based on the monotonic tension tests and the fitted Yld2000-2d yield function.

Fig. 5. True stress-strain curves in tension along the RD after prestraining in compression to (a) 2 % and (b) 4 % together with the stress-strain curve for monotonic tension. All curves are plotted up to necking.

Fig. 6. True stress-strain curves in uniaxial tension along every 15° from the RD. Dotted lines represent the monotonic true stress-strain curve in the same direction as the reloading. Dashed lines represent tension tests with 8% pre-deformation in tension along the RD, while solid lines represent tension tests with a further pre-deformation step by rolling in the TD. All curves are plotted up to necking.

Fig. 7. True stress-strain curves in tension along the RD after rolling in the TD to various strain levels and corresponding monotonic stress-strain curve. The true plastic prestrain by rolling is estimated by the von Mises strain. All curves are plotted up to necking.

Fig. 8. Comparison of the simulated and experimental stress-strain curves from tension tests prestrained by compression (2% and 4%) together with the monotonic loading curve.

Fig. 9. Experimental and simulated stress-strain curves in uniaxial tension at every 15° from the RD after 8% prestrain by uniaxial tension test in the RD and corresponding monotonic loading curve.

Fig. 10. True stress-strain curves in tension along the RD after rolling in the TD to various strain levels and corresponding monotonic stress-strain curve.

Fig. 11. Experimental and simulated (with the HAH model) maximum stress ratio for tension-tension tests at various angles from the RD.

Fig. 12. Kocks-Mecking plots for tension in the 60° direction with and without 8 % prestrain in tension along the RD and for tension along the RD with and without 12 % and 15 % prestrain by rolling in the TD.

Fig. 13. Stress ratio versus rolling prestrain at a total true plastic strain of 0.2 showing the degree of permanent softening. Results based on the rolling-tension tests in Fig. 7 and the tension-rolling tension tests in Fig. 6 are shown.

Table Captions:

Table 1. Normalized yield stresses and r-values from monotonic tension tests.

Table 2. Coefficients of the Yld2000-2d yield function.

Table 3. Model parameters for AA3103 alloy.